

**APPROACH IN ENHANCING THE FRACTAL ELECTRODES FOR INTERFACING
NEURONS USING QUANTUM STATE**

M Pavan Kumar

Research Scholar

Shri Jagadish Prasad Jhabarmal Technical University (JJTU)

marlapavankumar10@gmail.com

Dr. Prashanth Kumar Vaidya

Associate Professor, Internal Faculty

Shri Jagadish Prasad Jhabarmal Technical University (JJTU)

prashanthvaidya@yahoo.com

Dr. Sunil Dwivedi

Associate Professor

Shri Jagadish Prasad Jhabarmal Technical University (JJTU)

sunilas07@gmail.com

ABSTRACT

Electronically restoring vision to patients blinded by severe retinal degenerations is rapidly becoming a realizable feat through retinal implants. Upon receiving an implant, previously blind patients can now detect light, locate objects, and determine object motion direction. However, the restored visual acuity (VA) is still significantly below the legal blindness level ($VA < 20/200$). The goal of this research is to optimize the inner electrode geometry in photovoltaic subretinal implants in order to restore vision to a VA better than blindness level. We simulated neural stimulation by 20 μm subretinal photovoltaic implants featuring square or fractal inner electrodes by: (1) calculating the voltage generated on the inner electrode based on the amount of light entering the photodiode, (2) mapping how this voltage spreads throughout the extracellular space surrounding retinal bipolar neurons, and (3) determining if these extracellular voltages are sufficient for neural stimulation. By optimizing the fractal inner electrode geometry, we show that all neighboring neurons can be stimulated using an irradiance of $12 \text{ mW}/\text{mm}^2$, while the optimized square only stimulates $\sim 10\%$ of these neurons at an equivalent irradiance. The 20 μm fractal electrode can thus theoretically restore VA up to 20/80, if other limiting factors common to retinal degenerations, such as glia scarring and rewiring of retinal circuits, could be reduced. For the optimized square to stimulate all neighboring neurons, the irradiance has to be increased by almost 300%, which is very near the maximum permissible exposure safety limit. This demonstration that fractal electrodes can stimulate targeted neurons for long periods using safe

irradiance levels highlights the possibility for restoring vision to a VA better than the blindness level using photodiode-based retinal implants.

1.0 INTRODUCTION

Retinal prostheses aim to restore a degree of vision in patients with photoreceptor degeneration. The principle is either to take advantage of the surviving retinal circuitry or to target retinal ganglion cells (RGCs) directly, the output channels from the eye to the brain, encoding visual scenes into spike trains which are then transmitted to central visual targets via the optic nerve. Epi-retinal prostheses consist of micro-electrode arrays (MEAs) opposed to the vitreal side of the retina, providing direct electrical stimulation to the RGC layer. Individual electrodes have to deliver electrical pulses strong enough to elicit action potentials in surrounding RGCs without damaging the electrode material or the target tissue.

As the main interface between the prosthetic device and the tissue, electrodes are critically important components of any neuro-prosthetic system. For epi-retinal prosthetic devices, maximal resolution would ideally involve stimulation of individual RGCs, requiring electrode sizes to match those of their target neurons. However, small electrodes require higher charge densities to provide sufficient power to drive cells above firing threshold. If the charge density is too high, it can damage the tissue or the electrode, rendering the system unusable in the long term. Hence, it is important to estimate safe charge density limits based on electrode and tissue properties, allowing the system to function safely over prolonged periods. An optimal epi-retinal stimulation system would thus include very small, capacitive electrodes, located in close proximity to the RGC layer, requiring low amounts of current to depolarise RGCs to threshold. Small electrode dimensions guarantee stimulation localization and capacitive electrodes help avoiding direct charge injection into the tissue and undesired Faradaic reaction.

As charge density is intrinsically related to the effective surface area of the electrode, the geometry of stimulating electrodes strongly affects their charge density limit. As such, materials with large effective surface areas are ideal for efficient stimulation. Materials such as titanium nitride (TiN), iridium oxide (IrOx) and platinum grey are considered as gold standards for neural prosthetics and used respectively by the three main retinal prosthetic projects. Carbon nanotubes (CNTs) have attracted much attention since their emergence in the field of bioengineering due to their outstanding electrical, chemical and mechanical properties. Their high surface area,

remarkable tensile strength, biocompatibility and high conductivity make them an alluring candidate material to use in neural prosthetic electrodes .

Neuro degeneration is characterized by strong glial proliferation, and rejection of epi-retinal electrodes by glial cells can potentially widen the gap between electrodes and their target neurons, thus increasing the amount of charge required to elicit action potentials. The glial population of the retina, consisting of microglia (scattered throughout the inner retinal layers), astrocytes (horizontal syncytium at the nerve fibre layer) and Müller cells (spanning the retina transversely) maintain homeostasis , provide immunological protection and structural support . Macroglia (astrocytes and Müller Cells) are also the source of the inner limiting membrane (ILM), a basement membrane providing physical and electrostatic barrier between the vitreous and the retina.

2.0 LITERATURE REVIEW

Afshinmanesh F., Curto A. G., Milaninia K. M., van Hulst N. F., Brongersma M. L. (2014)

Existing epi retinal implants for the blind are designed to electrically stimulate large groups of surviving retinal neurons using a small number of electrodes with diameters of several hundred micrometers. To increase the spatial resolution of artificial sight, electrodes much smaller than those currently in use are desirable. In this study, we stimulated and recorded ganglion cells in isolated pieces of rat, guinea pig, and monkey retina. We used micro fabricated hexagonal arrays of 61 platinum disk electrodes with diameters between 6 and 25 μm , spaced 60 μm apart. Charge balanced current pulses evoked one or two spikes at latencies as short as 0.2 ms, and typically only one or a few recorded ganglion cells were stimulated. Application of several synaptic blockers did not abolish the evoked responses, implying direct activation of ganglion cells. Threshold charge densities were typically $0.1 \text{ mC}/\text{cm}^2$ for a pulse duration of 100 μs , corresponding to charge thresholds of 100 pC .

Ayton L. N., Blamey P. J., Guymer R. H., Luu C. D., Nayagam D. A. X., Sinclair N. C., et al. . (2014)

The dependence of a photodiode's performance on its top contact geometry is explored using modified nodal analysis. The results reinforce the need to balance a low mean semiconductor-metal separation distance with an adequate contact width for low resistance, all while maximizing light input. Future designs will benefit from the spatial voltage maps produced by the simulation. The electric field emanating from an electrode is also dependent on the

geometry of the electrode. The Faraday cage effect is exploited to achieve similar electric field responses to traditional electrode shapes.

Bank R. E., Rose D. J. (1981) With life expectancy on the rise, age-related ailments are a significant strain on the welfare of individuals and the economy. Progress is being made towards combating the leading cause of unavoidable blindness, age-related macular degeneration (AMD). AMD affects ten million Americans and costs the world economy 343 billion dollars annually. Retinal implants promise to restore sight by replacing the eye's damaged photoreceptors with electronic photodiodes. Clinical trials succeed at restoring some vision, but are limited by the stimulating electrodes. We study the electrode-neuron interface with a focus on the geometrical dependence of the electrode.

Bao Y.-J., Li H.-M., Chen X.-C., Peng R.-W., Wang M., Lu X., et al. (2008) The choice of electrode material is of paramount importance in neural prosthetic devices. Electrodes must be biocompatible yet able to sustain repetitive current injections in a highly corrosive environment. We explored the suitability of carbon nanotube (CNT) electrodes to stimulate retinal ganglion cells (RGCs) in a mouse model of outer retinal degeneration. We investigated morphological changes at the bio-hybrid interface and changes in RGC responses to electrical stimulation following prolonged *in vitro* coupling to CNT electrodes.

Bausch C. S., Koitmäe A., Stava E., Price A., Resto P. J., Huang Y., et al. (2013) By optimizing the fractal inner electrode geometry, we show that all neighboring neurons can be stimulated using an irradiance of 12 mW/mm², while the optimized square only stimulates ~10% of these neurons at an equivalent irradiance. The 20 μm fractal electrode can thus theoretically restore VA up to 20/80, if other limiting factors common to retinal degenerations, such as glia scarring and rewiring of retinal circuits, could be reduced. For the optimized square to stimulate all neighboring neurons, the irradiance has to be increased by almost 300%, which is very near the maximum permissible exposure safety limit. This demonstration that fractal electrodes can stimulate targeted neurons for long periods using safe irradiance levels highlights the possibility for restoring vision to a VA better than the blindness level using photodiode-based retinal implants.

3.0 METHODOLOGY

Implant fabrication

The photovoltaic arrays were designed based on the fabrication and operation principles published earlier, using an updated fabrication process and smaller pixel sizes. Implants of 1 mm in diameter and 30 μm in thickness consist of hexagonally arranged photovoltaic pixels. In a rat eye, these implants cover approximately 20° of the visual field. In the current study, pixels were either 40 or 55 μm in width, corresponding to 502 or 250 pixels in each array, respectively. Due to the hexagonal arrangement, spacing of the adjacent rows, i.e. pixel pitch, is 35 and 48 μm , respectively. Each pixel includes two diodes connected in series between the active (A) and return electrode (B) to maximize the efficiency of subretinal charge injection and stimulation. The diodes are fabricated on n- silicon substrate (phosphorus 10^{15} cm^{-3}) with p+ doping (boron 10^{19} cm^{-3}) and a junction depth of 1.5 μm .

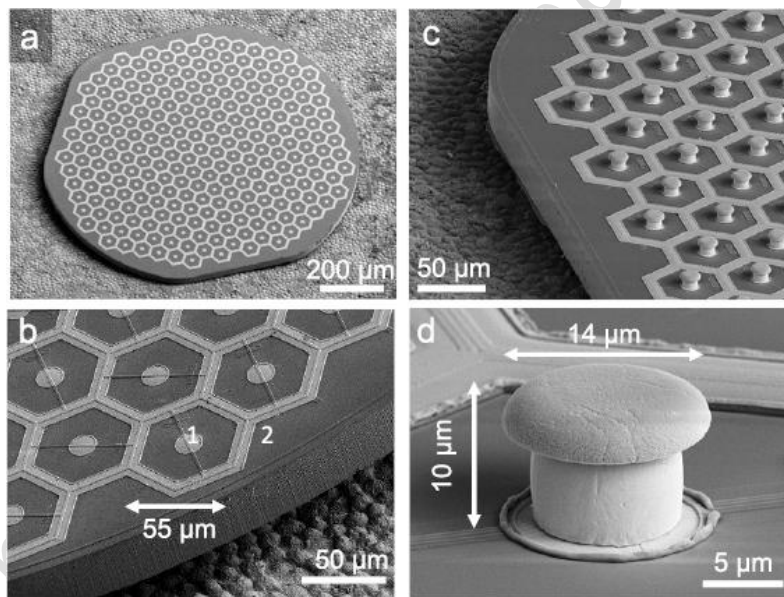


Figure Scanning electron micrographs (SEM) of the hexagonal photovoltaic arrays with 55 μm pixels. (a) The whole implant of 1 mm in width, containing 250 pixels. The array was placed on top of the RPE for scale. (b) Higher magnification of the implant demonstrates relative sizes of the central active electrode and circumferential return electrode in flat pixels. The active electrode is 14 μm in diameter, and return electrodes are 9 μm wide. (c) Similar array with pillar electrodes. (d) Image of a single pillar electrode with a SIROF-coated cap. The pillar is 10 μm in height, with a cap width of 14 μm and stem width of 10 μm .

Active electrodes are connected to the p⁺ regions, so that they develop a positive potential with respect to return electrode when the device is illuminated. To increase the photosensitive area compared to previous design, we minimized the width of the isolation trenches between diodes and between pixels to 1 μm . We also eliminated the 5 μm -wide open trenches between pixels, which were helpful in the previous implants for diffusion of oxygen and nutrients in *ex vivo* experiments but are not required *in vivo* due to presence of the retinal vasculature. Return electrodes connected across the entire array are shared across the pixel boundaries, and thereby cover the isolation trenches between pixels.

Active electrodes are 10 and 14 μm in diameter, and the width of the shared return electrode is 6 and 9 μm for 40 and 55 μm pixels, respectively (i.e. 3 and 4.5 μm per pixel), so that the area of the returns is about five times that of the active electrodes. Active and return electrodes were coated with sputtered iridium oxide film (SIROF) to create a high-capacitance electrode–electrolyte interface. To prevent the implant erosion and provide an antireflection coating, all implants were covered with 380 nm of amorphous silicon carbide (SiC) on top of 70 nm of silicon dioxide (SiO₂), optimized for 880 nm illumination.

Animals and implantation

Royal college of surgeons (RCS) rats was used as an animal model of inherited retinal degeneration. In these animals, a mutation in the MERTK gene reduces the phagocytic capability of the retinal pigmented epithelium (RPE), leading to degeneration of photoreceptors by four months. Rats were implanted after the loss of photoreceptors, and the follow-up continued for the life of the animals (up to one year). The animals were housed and maintained at the Stanford animal facility with a 12 h light/12 h dark cycle with food and water ad libitum.

Adult Long-Evans WT rats were purchased from Charles River Laboratories (Wilmington, MA, USA) as a wild-type control for measurements of the grating acuity ($n = 6$) and frequency response ($n = 5$). All *in vivo* experimental procedures were conducted in accordance with the Stanford University institutional guidelines and conformed to the guidelines of the Association for Research in Vision and Ophthalmology (ARVO) Statement for the Use of Animals in Ophthalmic and Vision research.

4.0 RESULTS

Stimulation thresholds

Response to prosthetic stimulation was evaluated by recording VEP via transcranial electrodes placed above the visual cortex, as described previously and exemplified in figure. A near-infrared beam (915 nm) reflected off the DMD, was projected onto the implant from a slit lamp. Stimulation thresholds with respect to irradiance and pulse duration, as well as variation of the VEP amplitude with frequency, were measured in the ranges summarized in table 1 (see methods). The VEP amplitude was quantified as the peak-to-peak voltage of the recording within 350 ms post stimulus, and amplitude greater than six times the RMS noise was considered a signal above threshold. Previous experiments demonstrated that VEP is not present when conduction along the optic nerve is blocked. We also verified that RCS rats do not respond to NIR flashes projected outside the implant.

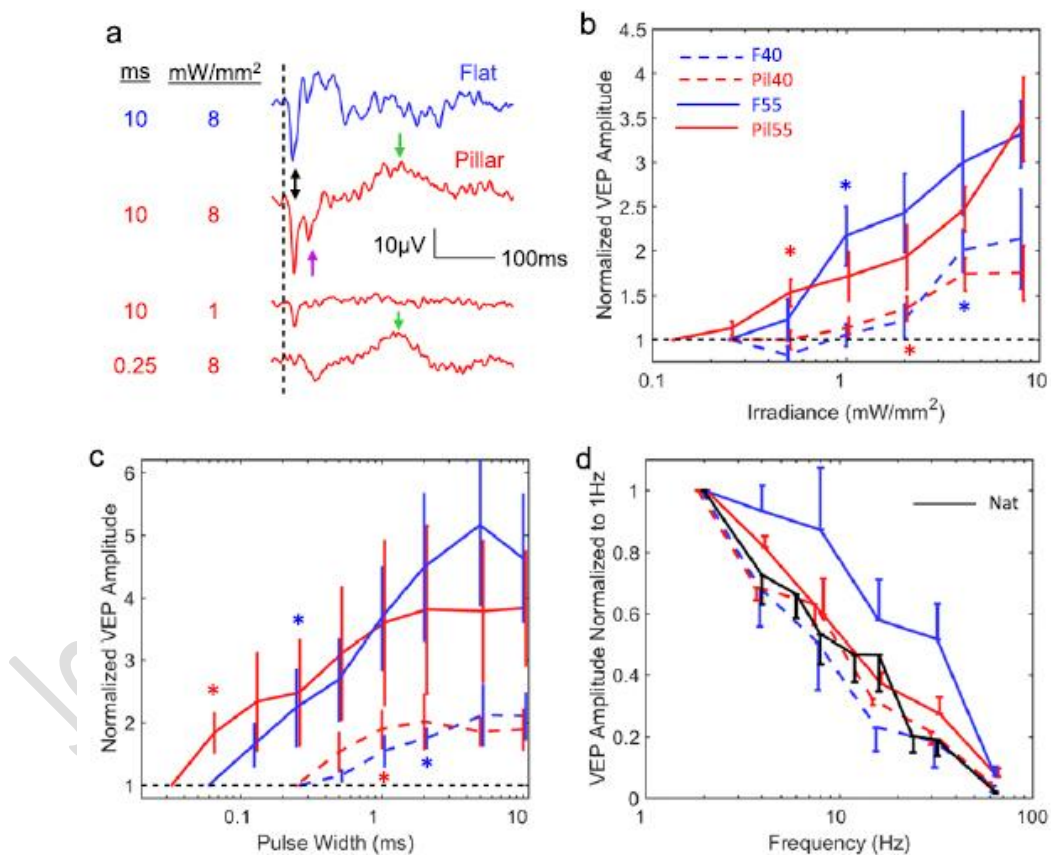


Figure Visually evoked potentials (VEP) and stimulation thresholds. (a) Example VEP waveforms with flat and pillar 55 μm implants at various irradiances and pulse durations. The traces were averaged over 500 trials. (b) Variation of the VEP amplitudes with

irradiance. (c) Variation of the VEP amplitudes with pulse width. (d) Variation of the VEP amplitudes with frequency.

irradiance. Stars indicate the lowest irradiance at which $p < 0.05$ (unpaired t -test, $n = 5$ for each implant type). (c) Variation of the VEP amplitude with pulse width. (d) Variation of the VEP amplitude with frequency for all 4 implant types and for normal vision ($n = 5$) F55 implants ($n = 5$) induced cortical response above $1.0 \pm 0.27 \text{ mW mm}^{-2}$ (s.e.m.), while with Pil55 implants ($n = 5$) the threshold was $0.55 \pm 0.15 \text{ mW mm}^{-2}$. The 45% decrease in stimulation threshold agrees with our previous modeling results. With increasing irradiance, the cortical response with flat implants maintained generally the same shape, while its amplitude increased with irradiance. Signals with pillar implants had a distinctly different shape: in addition to a short-latency negative peak at $\sim 20 \text{ ms}$ (double-headed arrow in figure), there was a second negative peak at $\sim 40 \text{ ms}$ and a positive peak about 100 to 200 ms later. The threshold of the second negative peak (purple arrow) was approximately an order of magnitude higher than that of the first negative peak.

The effect of pillars was much more pronounced on the threshold pulse duration: it decreased by 78%—from $0.29 \pm 0.11 \text{ ms}$ (s.e.m.) for F55 implants to $0.08 \pm 0.02 \text{ ms}$ for Pil55 arrays. The VEP of flat implants maintained the same shape as pulse duration varied, so that only the short ($\sim 20 \text{ ms}$) negative wave was detectable near the threshold. However, with pillars, the negative peak at 20 ms disappeared for very short pulses ($< 0.25 \text{ ms}$), while the much later positive component remained prominent.

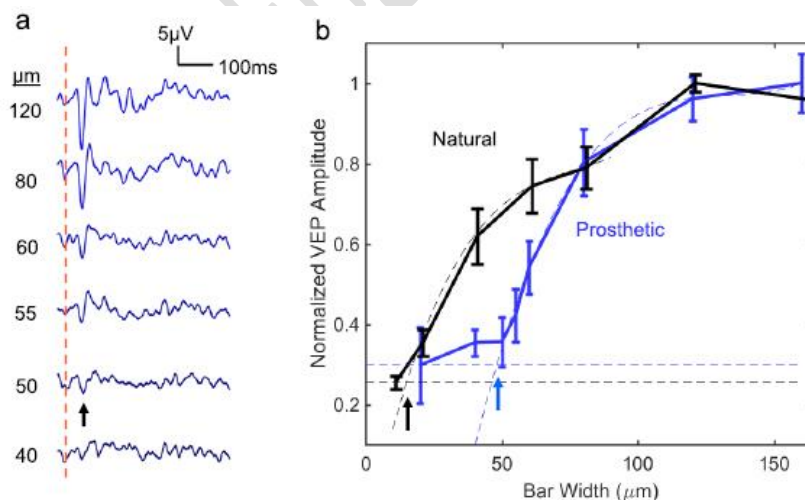


Figure Grating acuity. (a) Averaged prosthetic VEP response to alternating gratings with 55 μm pixels ($n = 5$). The red dash line indicates the instance of the grating reversal. (b)

Prosthetic and natural VEP amplitude as a function of the grating stripe width. Smaller stripe width corresponds to higher grating acuity.

Previous studies demonstrated that in healthy retina responding to pulsed visible light *ex vivo*, flicker fusion occurs at lower frequencies than in degenerate retina responding to prosthetic stimulation with 70 μm pixels. Our current measurements *in vivo* confirmed this effect for 55 μm flat implants, with the normalized VEP amplitude of prosthetic vision at 20 Hz being about twice that of natural, and reaching the same level beyond 50 Hz. Slower decline of retinal response with increasing frequency in prosthetic vision is likely due to absence of photoreceptors, the photochemical processes of which are much slower than the rest of the retinal network. However, with all pillar arrays and with 40 μm flat pixels, retinal response declined with frequency as fast as that of natural vision, suggesting another potential difference in the retinal stimulation mechanisms.

With F40 arrays ($n = 5$), the thresholds were significantly higher ($1.8 \pm 0.58 \text{ mW mm}^{-2}$ and $0.83 \pm 0.17 \text{ ms}$) and the maximum VEP amplitude about twice lower than that with 55 μm pixels. Even though the threshold is below the ocular safety limit (5 mW mm^{-2} average irradiance at 880 nm), not much range remains for encoding grey levels and assessing grating acuity, which requires a good signal-to-noise ratio achieved at irradiance levels far above the stimulation threshold. Pil40 arrays ($n = 5$) had thresholds of $1.3 \pm 0.27 \text{ mW mm}^{-2}$ and $0.7 \pm 0.12 \text{ ms}$, but this improvement did not result in increase of the maximum VEP amplitude—it was still only half that with 55 μm pixels. The effect of pillars on pulse duration with 40 μm pixels was also much smaller than with 55 μm .

Grating acuity

Measuring the cortical response to alternating gratings is an established method to assess visual acuity in animals and in human infants. Visual acuity measured with this method matches that of behavioral tests. We recorded the VEP response to alternating grating patterns projected onto the implant with 55 μm pixels in RCS rats. Images were delivered with NIR light at 8 mW mm^{-2} peak irradiance using 4 ms pulses at 40 Hz repetition rate, and pattern reversal at 1 Hz. The resulting VEP waveforms contained both a 2 Hz (pattern reversal-induced) and 40 Hz (pulse-induced) component. Using a 40 Hz notch filter, we singled out the pattern reversal-induced response, with its amplitude measured as the peak-to-peak voltage between 0 and 100 ms after

each pattern reversal. As a control, the same experiment was performed on healthy rats (Long Evans, $n = 6$) using green light (532 nm) illumination pulsed at 40 Hz.

The grating acuity limit was assessed by extrapolating the measured data down to noise level (see methods). Smaller grating width corresponds to better grating acuity. As can be seen in figure 4(b), for prosthetic vision with $55 \mu\text{m}$ pixels, this limit corresponds to $48 \pm 11 \mu\text{m}$ (s.e.m.). In a hexagonal array, adjacent rows are separated by $w = d \cdot \cos(30^\circ) = d\sqrt{3}/2 = 0.87d$, where d is the pixel width. For $d = 55 \mu\text{m}$, the distance between adjacent rows of pixels is $w = 48 \mu\text{m}$, matching the measured acuity. For natural vision, the measured grating acuity limit is $17 \pm 5 \mu\text{m}$. With $40 \mu\text{m}$ pixels, even having pillar electrodes, the VEP amplitude was too low for a reliable measurement of the grating acuity.

5.0 CONCLUSION

Our results demonstrate that hexagonal photovoltaic arrays with $55 \mu\text{m}$ pixels provide a grating acuity matching the minimum distance between adjacent rows, i.e. the Nyquist sampling limit of $48 \mu\text{m}$. Depending on the orientation of the grating, visual acuity with such arrays ranges from 20/192 to 20/220 in a human eye. If successful in human trials, prosthetic vision with such spatial resolution should benefit not only the patients blinded completely by inherited retinal degeneration (such as Retinitis Pigmentosa), but also much more patients with central vision loss due to advanced AMD.

Although the retinal circuitry undergoes drastic remodeling during the end-stage of degeneration, when all photoreceptors are lost, as in Retinitis Pigmentosa, recent clinical trials have demonstrated shape perception with subretinal electrical stimulation in RP patients. In AMD patients, photoreceptors are lost only within a few-mm-wide zone in the central macula, and the inner retinal structure is much better preserved in these areas, compared to the end-stage of RP. Therefore, restoration of central vision in AMD patients with subretinal implants might provide even better results, as evidenced by the recent success of the PRIMA implant. However, retinal degeneration may still limit the attainable visual acuity, and this effect remains to be tested with high resolution implants in clinical trials.

REFERENCES

1. Afshinmanesh F., Curto A. G., Milaninia K. M., van Hulst N. F., Brongersma M. L. (2014). Transparent metallic fractal electrodes for semiconductor devices. *Nano Lett.* 14, 5068–5074. 10.1021/nl501738b
2. Ayton L. N., Blamey P. J., Guymer R. H., Luu C. D., Nayagam D. A. X., Sinclair N. C., et al. . (2014). First-in-human trial of a novel suprachoroidal retinal prosthesis. *PLoS ONE* 9:e115239. 10.1371/journal.pone.0115239
3. Bank R. E., Rose D. J. (1981). Global approximate Newton methods. *Numerische Math.* 37, 279–295. 10.1007/BF01398257
4. Bao Y.-J., Li H.-M., Chen X.-C., Peng R.-W., Wang M., Lu X., et al. (2008). Tailoring the resonances of surface plasmas on fractal-featured metal film by adjusting aperture configuration. *Appl. Phys. Lett.* 92:151902 10.1063/1.2908972
5. Barone I., Novelli E., Piano I., Gargini C., Strettoi E. (2012). Environmental enrichment extends photoreceptor survival and visual function in a mouse model of retinitis pigmentosa. *PLoS ONE* 7:e50726. 10.1371/journal.pone.0050726
6. Bausch C. S., Koitmäe A., Stava E., Price A., Resto P. J., Huang Y., et al. (2013). Guided neuronal growth on arrays of biofunctionalized GaAs/InGaAs semiconductor microtubes. *Appl. Phys. Lett.* 103:173705 10.1063/1.4826885
7. Bethe H. A. (1944). Theory of diffraction by small holes. *Phys. Rev.* 66, 163–182. 10.1103/PhysRev.66.163
8. Beyeler M., Rokem A., Boynton G. M., Fine I. (2017). Learning to see again: biological constraints on cortical plasticity and the implications for sight restoration technologies. *J. Neural Eng.* 14:051003. 10.1088/1741-2552/aa795e
9. BrightFocus Foundation (2015). Sources for Macular Degeneration: Facts and Figures. Available online at: <https://www.brightfocus.org/sources-macular-degeneration-facts-figures> (Accessed November 21, 2016).
10. Butterwick A., Huie P., Jones B. W., Marc R. E., Marmor M., Palanker D. (2009). Effect of shape and coating of a subretinal prosthesis on its integration with the retina. *Exp. Eye Res.* 88, 22–29. 10.1016/j.exer.2008.09.018.